MODELLING SPRAY IMPINGEMENT ONTO FLAT, RIGID WALLS USING AN EULERIAN-LAGRANGIAN METHOD

F. Bierbrauer, T.N. Phillips

School of Mathematics, Cardiff University, Cardiff, CF24 4AG, UK

ABSTRACT

Liquid sprays are important in a range of industrial or engineering processes such as fuel injection in diesel engines or the spray painting of car door panels. It is often claimed that the characteristic impact behaviour of an individual spray droplet may be extrapolated to multiple droplets within the spray. Using a previously developed numerical model for the solution of multiphase flow problems it is shown that the impact behaviour of single and multiple droplets is very different, especially in the spreading and secondary droplet expulsion phase.

INTRODUCTION

Liquid sprays play an important role in many industrial processes: direct fuel injection in diesel engines, gas turbines, spray cooling of steel sheets, spray coating, spray painting and agricultural sprays [6]. A liquid is injected into an ambient gaseous medium as a fluid jet which often undergoes early break up as a consequence of cavitation within the injector exit holes [4]. These jets are further broken up into liquid sheets, ligaments and eventually droplets of varying sizes. This, atomised spray is now a dispersed liquid phase carried by a gaseous flow. Individual droplets within the spray can undergo further break up through aerodynamic forces characteristic of fluid dynamical instabilities on the phase dividing interface: the Rayleigh-Taylor and Kelvin-Helmholtz instabilities [11]. Individual droplets may also merge or coalesce and, if the spray is immersed within a heated environment, evaporate. Whether intentionally or unintentionally the resulting spray may impact onto solid surfaces causing secondary atomisation and the formation of a liquid film.

Spray-wall interaction is important in processes including the prevention of soil erosion due to rain, the underwater noise generated on the sea surface due to rain impingement [10] as well as the deposition of liquid fuel on cylinder walls leading to inefficient combustion as well as higher hydrocarbon emissions, particularly during engine warm-up [5]. Prediction of wall film thickness and average velocity is very important as these parameters are important when either trying to eliminate the deposited film, e.g. in combustion engines, or where maximum deposition is required, e.g. spray painting. Induced fluctuations within the liquid layer on rigid walls may also alter the quality of coated or painted surfaces [6]. Often it is the character of the atomised spray, such as droplet shape, size and impact velocity, that determines the spray/wall interaction. Impinging droplets may stick, bounce or break up into smaller ones through the splashing of individual droplets or the interaction of droplets with an already formed liquid layer [4].

Much of the previous literature on spray impact on rigid walls addresses droplet deposition, usually that of the normal impact of single droplets onto a dry or wetted wall. Prevailing models extrapolate the results of single droplet impact onto dry rigid walls to the case of spray-wall interaction by a superposition of many individual droplets [6]. However, recent research has shown that this limited approach neglects several important interactive effects such as: the influence of deposited film on secondary spray; the effect of film fluctuation on impacting droplets; the effect of multiple droplet interactions as well as the interaction of splash crowns and jets with other impacting drops [6].

Experimental measurements are often difficult to perform and experimental uncertainties can sometimes exceed the required sensitivity [4]. This makes the mathematical modelling of spray-wall interaction a viable alternative as well as allowing the investigation of individual fluid dynamical forces in the interaction process. These include inertial, viscous and capillary forces. The normal impact of individual droplets onto flat rigid walls has been modelled previously although the extension to multiple droplets and layer formation is lacking. It is the aim of this paper to study such multi-droplet interaction on flat rigid walls and examine how the resulting liquid layer influences further spray interaction. Spray parameters such as droplet size, shape and impact velocity will also be considered.

This paper will concentrate on the numerical modelling of the impact of multiple liquid droplets, within a gaseous medium, onto a flat rigid wall. In this paper we study the unsteady motion of two viscous, incompressible fluids with surface tension. Whereas the Level Set and Volume-of-Fluid (VOF) methods have been used in the past to simulate such multi-phase processes
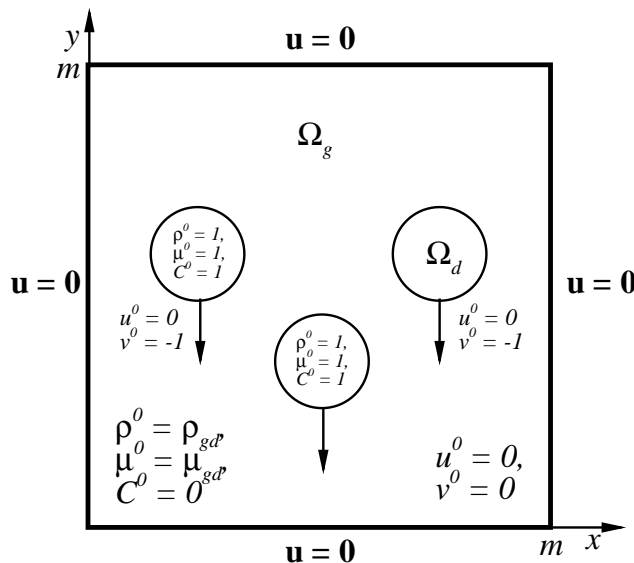
Figure 1: Configuration of the droplet impact problem

they possess certain well known weaknesses. Level Set methods have problems conserving mass as well as dealing with severe interfacial deformation whereas VOF methods cannot simulate fluid chunks which are smaller than the grid cell, a typical characteristic of dispersed flows. This paper uses the Marker-Particle method, an Eulerian-Lagrangian method which implicitly tracks fluid interfaces in a Lagrangian manner while maintaining fluid velocity and pressure on a fixed Eulerian grid. It uses an approximate Godunov projection method to conserve mass up to second order and is able to maintain individual fluid identity permanently at higher than grid resolution [1].

The aim of the paper is to study how the impact of multiple liquid droplets, making up the spray, onto a flat rigid surface affects the formation of wall films and how such impacts differ from previously used multiple, single impact models. These results form the first stage in the further study of the impact process. As such, the results demonstrate qualitative rather than quantitative behaviour of this process.

GOVERNING EQUATIONS

We consider a one-field formulation of the governing equations for unsteady incompressible flow. The non-dimensionalised Navier-Stokes (NS)equations are solved in the domain $\Omega = \{(x, y) : 0 < x, y < m\}$ with $\Omega = \Omega_g \cup \Omega_d$ where Ω_g represents the region of the domain occupied by the ambient gas and Ω_d that of the droplet fluid, see Figure 1. Thus, for two-phase flow, the governing equations written in dimensionless form

$$\frac{\partial \mathbf{u}}{\partial t} + (\mathbf{u} \cdot \nabla)\mathbf{u} = -\frac{1}{\rho}\nabla p + \frac{1}{\rho Re}\nabla \cdot \mu \mathbf{D} + \frac{\kappa(\mathbf{x})\nabla \rho}{We[\rho]\langle\rho\rangle} - \frac{\mathbf{j}}{Fr},$$
$$\nabla \cdot \mathbf{u} = 0,$$
$$\frac{\partial C}{\partial t} + \mathbf{u} \cdot \nabla C = 0,$$
$$\rho = C + (1 - C)\rho_{ad},$$
$$\mu = (C + (1 - C)/\mu_{ad})^{-1}$$

$$(1)$$

where $\mathbf{D} = \nabla\mathbf{u} + \nabla\mathbf{u}^T$ and we have non-dimensionalised with respect to: length-initial droplet diameter D_d, velocity-initial droplet impact velocity U_d, density-droplet density ρ_d, viscosity-droplet viscosity μ_d, pressure-$\rho_d U_d^2$ and time-the convective time D_d/U_d scale. The Reynolds, Weber and Froude numbers are defined by $Re = \rho_d U_d D_d/\mu_d$, $We = \rho_d U_d^2 D_d/\sigma_{gd}$ and $Fr = U_d^2/gD_d$. The density and viscosity ratios are: $\rho_{gd} = \rho_g/\rho_d$, $\mu_{gd} = \mu_g/\mu_d$. The volume fraction $C = C_d$ so that $C_a = 1 - C_d$. The surface force term is expressed through the curvature $\kappa(\mathbf{x}) = \nabla \cdot \mathbf{n}$ where $\mathbf{n} = \nabla\rho/|\nabla\rho|$ is the normal to the interface, the jump in density across the interface is $[\rho] = 1 - \rho_{gd}$ and average of the densities is given by $\langle\rho\rangle = (1 + \rho_{gd})/2$. Dimensional domain lengths are L taken as an integer multiple of droplet diameter, $m = L/D_d$.

Boundary conditions are no-slip walls, $\mathbf{u}|_{\partial\Omega} = \mathbf{0}$, along all boundaries. This allows the study of a confined space where fluid layers can build up on the impacted wall. No flux conditions on the density, viscosity and consequently the volume fraction are used for all boundaries, i.e. $\mathbf{n} \cdot \nabla\rho|_{\partial\Omega} = \mathbf{n} \cdot \nabla\mu|_{\partial\Omega} = \mathbf{n} \cdot \nabla C|_{\partial\Omega} = 0$. Note that the flow is fully two-dimensional without use of symmetry conditions along the plane of symmetry.

Although no pressure boundary conditions are required, projection methods make use of a gauge variable ϕ to ensure satisfaction of an approximate solenoidal velocity field. Gauge variable boundary conditions are homogeneous Neumann conditions $\mathbf{n} \cdot \nabla\phi|_{\partial\Omega} = 0$. Initial densities and viscosities were constant in each fluid and all initial pressures were zero. Initially, we prescribe $\mathbf{u}^0 = \mathbf{i}$ in the ambient fluid and $\mathbf{u}^0 = \mathbf{0}$ in the droplet, see Figure 1.

THE NUMERICAL METHOD

The semi-implicit projection method

The system (1) is solved using the approximate Godunov projection method [8] with second-order Crank-Nicolson time discretisation. Given the strengths and weaknesses of the various projection methods we choose to use a modified version of the incremental pressure projection method of Rider *et al.* [9]. The original method uses a time-lagged discretization of the pressure gradient in the momentum equation, sets the intermediate velocity boundary conditions to the physical boundary conditions and uses a homogeneous

2

Neumann condition in the projection stage of the algorithm. The modification to this method uses a corrected pressure update to ensure consistency and incorporates a variable density.

In semi-discrete form, this results in the following pressure corrected, variable density, second-order approximation of the equations (1) at time t^n:

1. Step 1: Given $\mathbf{u}^n$, $\nabla p^{n-1/2}$, ρ^n, μ^n, C^n calculate $(\mathbf{u} \cdot \nabla \mathbf{u})^{n+1/2}$

2. Step 2: update C^{n+1} so that
$$\begin{aligned} \rho^{n+1} &= C^{n+1} + (1 - C^{n+1})\rho_{ad}, \\ \mu^{n+1} &= \left(C^{n+1} + (1 - C^{n+1})/\mu_{ad} \right)^{-1} \end{aligned} \quad (2)$$

and define $\rho^{n+1/2} = (\rho^n + \rho^{n+1})/2$ and $\mu^{n+1/2} = (\mu^n + \mu^{n+1})/2$.

3. Step 3: solve for the intermediate velocity
$$\begin{aligned} &\left(\mathbf{I} - \tfrac{\Delta t}{2Re}\sigma^{n+1/2} L_\mu^{n+1/2}\right) \mathbf{u}^* = \left(\mathbf{I} + \tfrac{\Delta t}{2Re}\sigma^{n+1/2} L_\mu^{n+1/2}\right) \mathbf{u}^n \\ &- \Delta t \left((\mathbf{u} \cdot \nabla \mathbf{u})^{n+1/2} + \sigma^{n+1/2}\nabla p^{n-1/2} - \sigma^{n+1/2}\mathbf{F}^{n+1/2} \right) \end{aligned} \quad (3)$$

4. Step 4: project the result
$$L_\sigma^{n+1/2} \phi^{n+1} = \tfrac{1}{\Delta t}\nabla \cdot \mathbf{u}^* \quad (4)$$
followed by
$$\mathbf{u}^{n+1} = \mathbf{u}^* - \Delta t \sigma^{n+1/2}\nabla \phi^{n+1} \quad (5)$$

5. Step 5: update the pressure gradient
$$\begin{aligned} \nabla p^{n+1/2} = & \ \nabla p^{n-1/2} + \nabla \phi^{n+1} - \\ & \tfrac{\Delta t}{2Re}L_\mu^{n+1/2}\left(\sigma^{n+1/2}\nabla\phi^{n+1}\right) \end{aligned} \quad (6)$$

where $\mathbf{F} = \kappa(\mathbf{x})\rho\nabla\rho/(We[\rho]\langle\rho\rangle) - \rho\mathbf{j}/Fr$ and the Laplacian operators are given by $L_\mu \mathbf{w} = \nabla \cdot \mu(\nabla\mathbf{w} + (\nabla\mathbf{w})^T)$, for a vector $\mathbf{w}$, and $L_\sigma \psi = \nabla \cdot \sigma\nabla\psi$, for a scalar ψ, $\sigma = 1/\rho$, $\sigma^{n+1/2} = (\sigma^n + \sigma^{n+1})/2$ and $\bar{\Omega} = \Omega \cup \partial\Omega$. The determination of the $(\mathbf{u} \cdot \nabla \mathbf{u})^{n+1/2}$ term in Step 1 represents an approximation to the nonlinear advection term at the half time level and is the one detailed in [8]. The velocity at the half time level has also been used in the viscous term and is given by $\mathbf{u}^{n+1/2} = (\mathbf{u}^n + \mathbf{u}^*)/2$. The extra pressure correction term $-(\Delta t/2Re)L_\mu\sigma\nabla\phi$ was obtained by eliminating the intermediate velocity in the momentum equation (3) using the update given by (5).

Note that in the projection method described above the time updated density and viscosity are required in Step 1 where only the values at the nth time level are known. This is calculated with the use of the Godunov Marker-Particle Projection Scheme (GMPPS) [2] where fluid particles are advanced forward in time to track individual fluid phases while carrying particle colour information. The time updated volume fraction for the fluid phase C^{n+1} is then obtained by interpolation from surrounding fluid particles of that phase. This provides the solution of the advection equation for the volume fraction.

The smoothing of discontinuities

Since there are discontinuities in the physical properties, such as density and viscosity, an element of smoothing is necessary. In practice, the volume fraction is smoothed by forming the convolution of C with a kernel $K(\mathbf{x}; \epsilon)$ which becomes the surface delta function as $\epsilon \to 0$ [3], i.e.

$$\tilde{C}(\mathbf{x}) = \int_{\Omega_K} C(\mathbf{x}')\mathbf{K}(r; \varepsilon)\, d\mathbf{x}' \quad (7)$$

where $r = |\mathbf{x}' - \mathbf{x}|$. Here, Ω_K is the compact support of the kernel, or the points for which $\mathbf{K}(r; \varepsilon) \neq 0$ and ε the size of the support. Ideally, a kernel should possess compact support, be monotonically decreasing with respect to r, be radially symmetric, be sufficiently smooth, be a good representation of the delta function as $|\Omega_K| \to 0$ and possess the normalisation property $\int_{\Omega_K} \mathbf{K}(r; \varepsilon)\, d\mathbf{x} = 1$ [12]. In the present case we choose the eighth degree polynomial kernel because it closely matches all of the properties listed above, being superior to say the Nordmark kernel which is not monotonically decreasing and tends to produce highly singular oscillations as $|\Omega_K| \to 0$ [12]. The kernel is defined by

$$\mathbf{K}_8(r; \varepsilon) = \begin{cases} \frac{5}{\pi \varepsilon^2}[1 - (r/\varepsilon)^2]^4 & \text{if } r < \varepsilon \\ 0 & \text{otherwise} \end{cases}$$

At any point (x, y) in the domain the volume fraction may be convolved by considering a circle of radius ε, $(x'-x)^2 + (y'-y)^2 = \varepsilon^2$, the support of the kernel, and integrating (7). The evaluation of this integral requires a little care when examining points near the boundary, within one cell width, as the support of the kernel may overlap the boundary therefore requiring ghost cells as part of the evaluation. A finite number of ghost cells indicates that the smoothing length should not exceed two to three cell widths.

Spatial discretisation of differential operators

We use a collocated grid defined in [2] for the velocity and pressure $\mathbf{u}_{i,j}$, $p_{i,j}$ for $i = 1, 2, 3, ..., I$, $j = 1, 2, 3, ...J$ with cell edges used to define the boundaries at $x_{1/2}, y_{1/2} = 0$, $x_{I+1/2}, y_{J+1/2} = m$. Discrete differential operators are second order accurate cell-centred discretisations as detailed in [3]. The discretised convective term in the NS equations is given in [8]. Boundary conditions are imposed along the left, right, top and bottom most cell edges and determine ghost cell values required by the discretisation. Time step restrictions include a CFL condition as well as terms involving the various forces acting

$$\Delta t < \frac{1}{2} \min_{\substack{1 \le i \le I \\ 1 \le j \le J}} \left(\frac{\Delta x}{|u_{i,j}^n|}, \frac{\Delta y}{|v_{i,j}^n|}, \frac{3Re}{14}\frac{\rho_{i,j}^n(\Delta x^2, \Delta y^2)}{\mu_{i,j}^n}, \right.$$
$$\left. \sqrt{\frac{2(\Delta x, \Delta y)}{F_{i,j}^n}} \right) \quad (8)$$

where

$$F_{i,j}^n = \left| -\sigma_{i,j}^n (\mathbf{G}p)_{i,j}^{n-1/2} + \frac{\sigma_{i,j}^n}{Re}(L_\mu \mathbf{u})_{i,j}^n \right.$$

$$\left. + \frac{\kappa_{i,j}^{n+1/2}(\mathbf{G}\rho)_{i,j}^{n+1/2}}{We[\rho]\langle\rho\rangle} - \frac{1}{Fr}\hat{\mathbf{j}} \right|$$

Filtering of velocity data

One of the drawbacks associated with approximate projection methods on collocated grids is the existence and growth of null spaces in the discrete divergence operator giving rise to 'checkerboard modes' where the discrete operator fails to recognise non-divergence-free modes [9]. This is manifested as high frequency noise in the discrete divergence of the velocity. Through the use of iterated projection filters, which diffuse divergent modes, and velocity filters, which subtract off unphysical modes from the velocity field, these spurious modes are mostly removed [9]. Filters are best used in conjunction at the end of a computational cycle and are essential for two-phase flows with large density ratios which, if not applied, create spurious velocity fields showing noise, asymmetry and eventually instability [9, 7]. Both projection and velocity filters are used in this paper.

NUMERICAL RESULTS

Recent work has suggested that previous assumptions about spray impact are not admissible. One such assumption states that the impact behaviour of a single droplet onto a flat surface may be used to model the behaviour of multiple droplets. In other words it is assumed that droplet-droplet interaction plays little role in spray impact behaviour. The following investigation tests the validity of this assumption by simulating the impact of: (i) a single droplet, (ii) two isolated droplets of the same size, (iii) three droplets of the same size with the central one positioned slightly closer to the surface, (iv) three droplets, two of the same initial diameter and the central one 4/3 larger than the other two, (v) three droplets, two of the same initial diameter and the central one 3/4 of the size of each of the other two. In all cases considered $D_d = 0.001$m, $\rho_d = 1000$ kg/m^3, $\mu_d = 0.001$ kg/ms, $\sigma_{gd} = 0.072$ N/m and $g = 9.81$m/s^2. The calculations take place inside a domain of size $10D_d \times 5D_d$ with a 256×128 grid. In the following set of graphical results, the impact plots show the $C = 1/2$ contour which best matches the interface position. All individual figures are read left to right, top to bottom. The total simulation time was $t = 5$ non-dimensional time units with a total of 20 time steps saved over this range. Each plot is taken at the 0, 5, 10, 15 and 20th saved time step.

$We = 13$

This case considers the impact of droplets with an initial impact velocity of $U_d = 1$ m/s giving a Weber number of $We = 13$. This case investigates how strongly surface forces influence the impact.
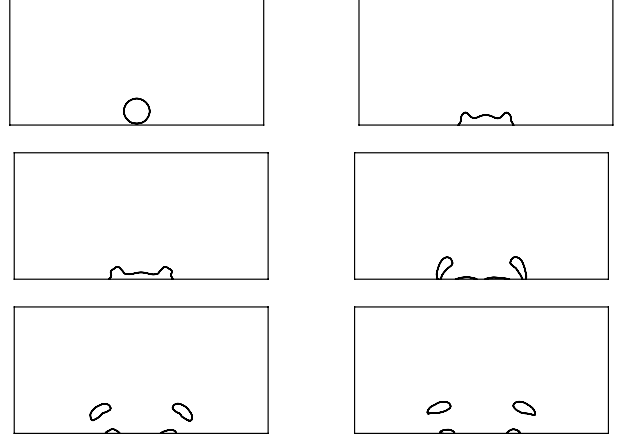

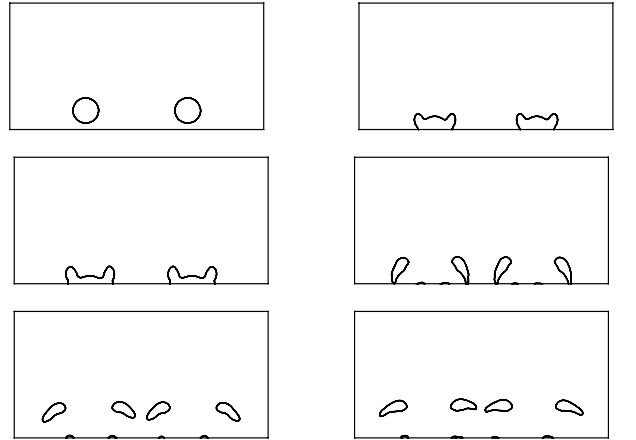Figure 2: The impact of a single water droplet for $We = 13$, $Re = 1000$

Figure 3: The impact of two isolated water droplets for $We = 13$, $Re = 1000$

$We = 1388$

This case considers the impact of a droplet with initial impact velocity of $U_d = 10$ m/s giving a Weber number of $We = 1388$. In this case the effect of surface forces is expected to be negligible.

DISCUSSION AND CONCLUSIONS

We discuss the results by first comparing the behaviour of the various impact scenarios for the $We = 13$ case where surface forces are expected to play a major role.
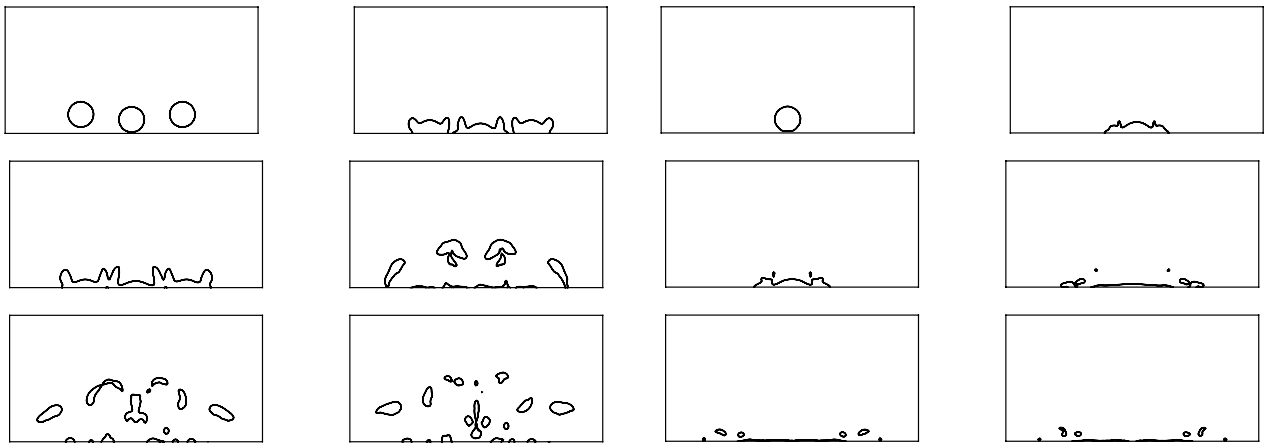
Figure 4: The impact of a three water droplets, reference configuration, for $We = 13$, $Re = 1000$

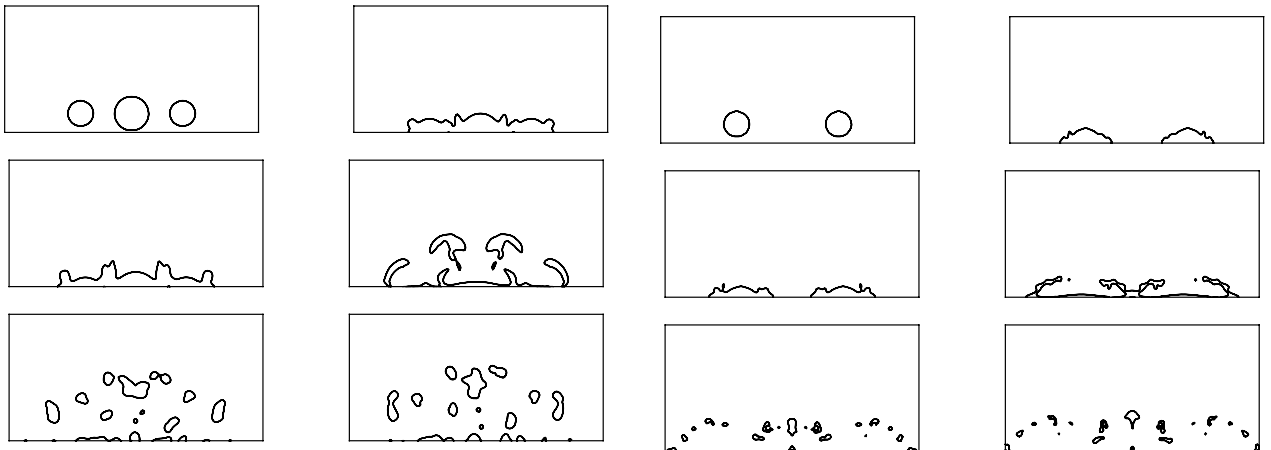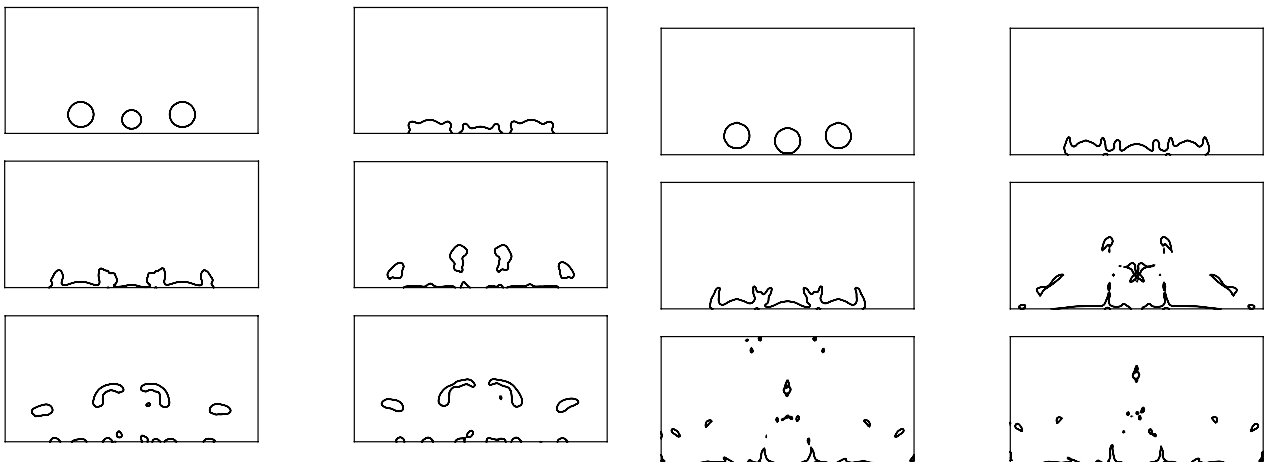Figure 5: The impact of a three water droplets, large central drop configuration, for $We = 13$, $Re = 1000$

Figure 6: The impact of a three water droplets, small central drop configuration, for $We = 13$, $Re = 1000$

The second case on the other hand, where $We = 1388$, should be more influenced by inertial forces.

Figure 7: The impact of a single water droplet for $We = 1388$, $Re = 10000$

Figure 8: The impact of two isolated water droplets for $We = 1388$, $Re = 10000$

Figure 9: The impact of a three water droplets, reference configuration, for $We = 1388$, $Re = 10000$
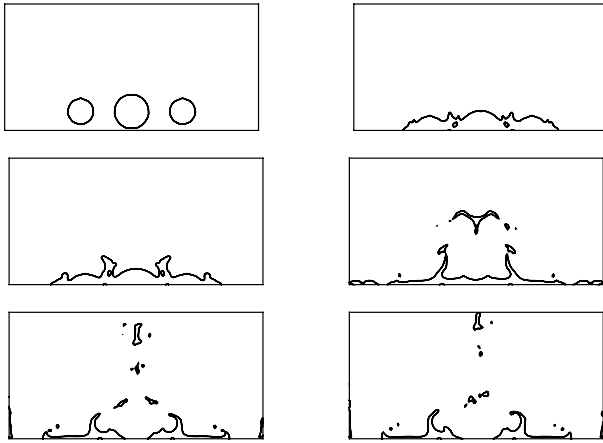
1. <u>$We = 13$</u>

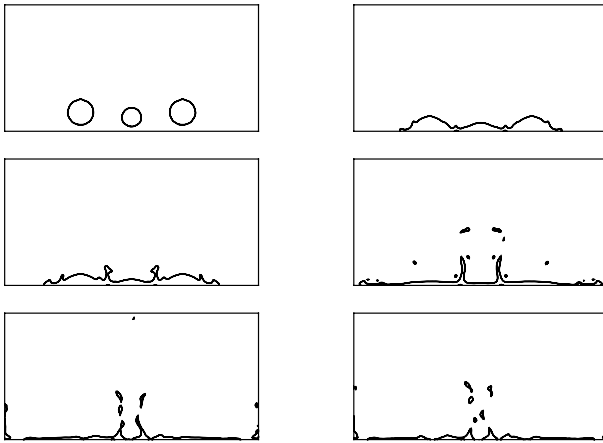Figure 10: The impact of a three water droplets, large central drop configuration, for $We = 1388$, $Re = 10000$

Figure 11: The impact of a three water droplets, small central drop configuration, for $We = 13$, $Re = 1000$

(a) *comparison of single and isolated droplets*: it is clear from Figures 2 and 3 that the impact behaviour of a single drop is very similar, if not the same as, that of two relatively isolated droplets. Each shows an initial spreading phase just after impact followed by the expulsion of secondary droplets. Figure 3 shows that the behaviour of the secondary droplets is very similar to that of the single droplet of Figure 2. It seems clear that, provided two individual droplets are far enough separated initially, their behaviour may be deemed to be explained by that of a single droplet.

(b) *comparison of single and multiple droplets*: a comparison of Figures 2 and 4 shows that just after impact, in the spreading phase, the central droplet is influenced by that of the two neighbouring droplets on either side. The spreading of the central droplet is confined

to some degree by the expanding rim of each of the other two. The character of the expulsion of secondary droplets is now quite different from that of a single droplet especially in the centre of the plot where a set of two large secondary droplets are not like those seen in Figure 3 although the droplets to the left and right-most sides show similar behaviour to that seen in Figure 3.

(c) *comparison of reference and large/small impact cases*: Figures 5 and 6 show the impact behaviour of three droplets where the central one is either larger or smaller than either of its neighbours. It is clear from Figures 4 and 5 that the extra volume of a central droplet allows a rapid expansion of the central droplet in the expansion phase and interacts with the two on either side earlier than for a central droplet with equal volume. The central droplet then dominates the expulsion of secondary droplets generating a larger set of these droplets than seen in Figure 4. Interestingly, when the central droplet possesses a smaller volume than the other two the impact behaviour tends to spread the mass to either side of the symmetry line. Most of the central mass is now expelled into two large secondary droplets.

2. $\underline{We = 1388}$

(a) *comparison of single and isolated droplets*: in this case, Figures 7 and 8 show that even the behaviour of the single and isolated droplets is very different. This time the expanding rim of the two droplets in the isolated case interact strongly preventing the characteristic spreading behaviour seen in Figure 7. Small secondary droplets are now seen to be expelled above the surface like a mist.

(b) *comparison of single and multiple droplets*: the extra energy present in this reference case of three equal sized impacting droplets, seen in Figure 9, indicates that while the initial impact behaviour is quite similar to that seen in Figure 4 large secondary droplets can no longer form. The remaining mass of the droplets is either greatly spread out or expelled above the surface into very small secondary droplets.

(c) *comparison of reference and large/small impact cases*: both Figures 10 and 11 show impact behaviour different from that of Figure 9. In the case with a larger central droplet a good deal of the mass is expelled above the symmetry line while the boundary conditions now influence the result more significantly with much of the mass being reintegrated into

the formation of a crater with high walls. The case with a smaller central droplet is more similar to that shown in Figure 9 although the two main secondary droplets are concentrated near the centre of the domain rather than to either side.

Two main conclusions are evident. Firstly, both the initial spreading phase and the expulsion of secondary droplets from the impact site for the case of single and multiple droplets shows very different behaviour. Secondly, the extra energy available in the $We = 1388$ case tends to expel both more and smaller secondary droplets than the $We = 13$ case where surface forces are no longer capable of holding fluid masses together against inertial forces. Whereas the $We = 13$ case generates large secondary droplets more of the mass is expelled as a mist in the $We = 1388$ case while the rest is confined to the surface.

NOMENCLATURE

Symbol	Quantity	SI Unit
$\mathbf{u}$	Velocity	m/s
p	Pressure	kg/ms^2
ρ	Density	kg/m^3
μ	Viscosity	Ns/m^2
C	Volume fraction	dimensionless
σ	Surface tension	N/m

References

[1] F. Bierbrauer and T.N. Phillips. The numerical prediction of droplet deformation and breakup using the Godunov marker-particle projection scheme. *Int. J. Numer. Methods Fluids*, 56:1155–1160, 2008.

[2] F. Bierbrauer and S.-P. Zhu. A numerical model for multiphase flow based on the GMPPS formulation, part I: kinematics. *Comput. Fluids*, 36:1199–1212, 2007.

[3] F. Bierbrauer and S.-P. Zhu. A numerical model for multiphase flow based on the GMPPS formulation, part II: dynamics. *Eng. Appl Comput. Fluid Mech*, 2:284–298, 2008.

[4] T. Bo, D. Clerides, A.D. Gosman, and P. Theodossopoulos. Multidimensional modelling of diesel combustion and emissions formation. Proc 1st Meet. Greek Section Combust. Inst., Athens, Greece, November 28-29 2007.

[5] M. Gavaises, A. Theodorakakos, and G. Bergeles. Modeling wall impaction of diesel sprays. *Int. J. Heat Fluid Flow*, 17:130–136, 1996.

[6] D. Kalantari and C. Tropea. Spray impact onto flat and rigid walls: Empirical characterisation and modelling. *Int. J. Multiphase Flow*, 33:525–544, 2007.

[7] D.B. Kothe. *Free Surface Flows*, pages 267–331. Springer, New York, 1999.

[8] E.G. Puckett, A. Almgren, J.B. Bell, D.L. Marcus, and W.J. Rider. A high-order projection method for tracking fluid interfaces in variable density incompressible flows. *J. Comput. Phys*, 130:269–282, 1997.

[9] W.J. Rider, D.B. Kothe, S.J. Mosso, J.H. Cerutti, and J.I. Hochstein. Accurate solution algorithms for incompressible multiphase flows. 33rd Aerospace Sciences Meeting, Reno, NV, US, November 28-29 1995.

[10] D.W. Stanton and C.J. Rutland. Multidimensional modeling of thin liquid films and spray-wall interactions resulting from impinging sprays. *Int. J. Heat Mass Transfer*, 41:3037–3054, 1998.

[11] F.X. Tanner. Liquid jet atomization and droplet breakup modeling of nonevaporating diesel fuel sprays. *J. Engines*, 106:127–140, 1998.

[12] M.W. Williams, D.B. Kothe, and E.G. Puckett. Convergence and accuracy of kernel-based continuum surface tension models. Proc 13th US Natl Congress of Appl Mech, Gainesville, Florida, USA, June 16-21 1998.